

Final Draft
of the original manuscript:

Pein, J.U.; Grayek, S.; Schulz-Stellenfleth, J.; Stanev, E.V.:
**On the impact of salinity observations on state estimates in
Ems Estuary**
In: Ocean Dynamics (2016) Springer

DOI: 10.1007/s10236-015-0920-0

On the impact of salinity observations on state estimates in Ems Estuary

Pein, JU; Grayek, S; Schulz-Stellenfleth, J;
Stanev EV

the date of receipt and acceptance should be inserted later

Abstract The hydrodynamics of Ems Estuary are dominated by tides and their interaction with buoyancy forcing. Such an environment is challenging for any effort to bring together observations and model results. In this study we investigate how salinity measurements in the Ems Estuary affect the reconstruction of the salinity field. Similar to the traditional Observing System Experiments, the impact of specific observational arrays is simulated in the framework of statistical experiments. The experimental algorithm mainly relies on the model covariance matrix. Each experiment results in an estimate of the reconstruction error. The analysed observation configurations involve single and multiple, as well as stationary and non-stationary observing arrays. Generally the reconstruction of the ocean state improves with increasing the density of observations. It appears certain locations are more favourable for reconstruction than others. In fact, the regions separating the main dynamical realms “resist” strongest to the reconstruction effort. Extending the covariance matrix by the temporal cross-covariances between the model grid points, enables to evaluate the impact of observations taken from a moving platform. This approach further improves the outcome of the experiments, resulting in reconstruction errors near zero with the exception of the tidal river. The

Address(es) of author(s) should be given

cross-covariance information is able to tackle even the irregular dynamics arising on the border between the different physical regimes.

Keywords: assessment of observing networks; observing system experiments; tidal dynamics; baroclinicity; moving observation platform; temporal cross-covariances

1 Introduction

The study of hydrodynamical processes in the ocean is based on both modelling and observation of the ocean state. Although both disciplines contribute to oceanography independently, they also profit significantly from one another: Observational data serve to validate numerical models, and measuring campaigns and observing networks are planned with the help of model results. In data assimilation both sources are merged into a single product. The basic idea of data assimilation is to regularly update a numerical model with observational data (Kalman 1960; Brasseur and Verron 2006). Given a sufficiently realistic numerical model and reliable observations, the joint product approximates the real state of the ocean or atmosphere better than the respective single sources. Apart from the quality of the model or the observations, the success of data assimilation depends on the ability of the assimilation algorithm to synergise the error statistics of the single sources. These error statistics are not necessarily compatible. Some measuring systems resolve physical scales which are much finer than the resolution of a numerical model. On the other hand it is not possible and not reasonable to deploy probes in every corner of the target area. These challenges motivate ongoing efforts to reduce the uncertainties associated with either source with the help of data assimilation.

Prior to the actual data assimilation process the questions has to be answered 1) which scales the observing network shall record and communicate to the model, 2) where the probes should therefore be taken. To answer this question, some effort

has been designated to the experimental assessment of observing networks (e.g. Arnold and Dey 1986).

The standard technique to assess the impact of an array of measuring devices on the assimilation system uses the Observing System Experiments (OSE) and Observing System Simulation Experiments (OSSE) (e.g. Arnold and Dey 1986; Ballabrera-Poy et al. 2007). Both assimilate data experimentally. In doing so, they quantify the representativeness of an observing network by including or excluding specific variables, observing instruments or stations. In the case of OSE existing observations are assimilated, whereas in the case of OSSE data sampled from a numerical model serves as synthetic observations. The crucial information needed from the real or simulated observing system are its associated errors. These can be systematic or random. Random errors relate to instrument noise or unresolved scales. The latter are referred to as representation errors (Oke and Sakov 2008), whereas the former is a technical property of the observing instrument. For the OSSE these biases need to be generated artificially and added to the samples (Arnold and Dey 1986). After assimilating the real or simulated observations into the model, the reconstructed state is compared to the reference state, i.e. the state without assimilated data. The less the difference between the so-called twin runs, the better the observing system.

Departing from the original idea of testing the observing network with the help of assimilation experiments, several studies proposed simplified approaches to assess the impact of observation strategies (Ngodock et al. 2006; Le Hénaff et al. 2009). For example, Schiller et al. 2004 assessed the representativeness of sampling strategies of ARGO floats by solely using proxy data from a numerical model. They demonstrated that spatial sampling had the greatest influence on the statistical significance of the samples.

The approach introduced by Schulz-Stellenfleth and Stanev 2010 integrates the Kalman filter theory and the definition of the reconstruction error in terms of a signal-to-noise ratio. Instead of assimilating observations into the model, they

reconstructed the ocean state from sparse observations adopting an approximation of the state covariance matrix. The method quantifies the reconstruction error as the deviation between the reconstructed state and the reference state. Grayek et al. 2015 further used this method to estimate the representativeness of individual locations in the model area. This approach results in quantitative information about how the inner correlation structure of a physical system can be optimally captured. The knowledge about the dynamical relations and features within a physical system is considered crucial for successful monitoring of the ocean state (Ballabrera-Poy et al. 2007). In our study we apply the tool-set of Schulz-Stellenfleth and Stanev 2010 and Grayek et al. 2015 for the purpose of assessing observation strategies of the salinity field in the region of Ems Estuary.

Among the numerous variables defining the ocean dynamics salinity is a valuable diagnostic one both at large scales (Tranchant et al. 2008) and estuarine scales (Pein et al. 2014). At the latter scales it is transported by the tides. On the other hand, it itself drives the estuarine and ocean dynamics via baroclinic currents (Talke et al. 2009; Huijts et al. 2006). In this sense, salinity constitutes an important prognostic variable.

Our aim is to investigate the impact of distinct spatial and temporal observation strategies on the overall knowledge about the distribution of the 3D salinity field. We want to answer the questions 1) to which degree can the state be reconstructed based on single, sparse or continuous observations and 2) which are the most important regions to be monitored. Furthermore, we aim to investigate the impact of moving observing platforms. In the following section we will introduce the methods employed in this study. In the results section we will report on the outcome of the statistical assessment and we will give a physical explanation of these results. The final two sections comprise the discussion of our results in the light of the related literature and the conclusions to this study.

2 Methods

2.1 The numerical model

Based on the theory of Kalman-filter and taking into consideration the recent development of the OSE and OSSE (see e.g. Oke and Sakov 2008; Schiller et al. 2004), a new technique of assessing ocean observing networks has been introduced by Schulz-Stellenfleth and Stanev 2010, which Grayek et al. 2015 named Statistical Evaluation of Observing Networks (SEON) in case of the assessment using real observations or Statistical Evaluation of Simulated Observing Networks (SESON) in case of synthetic observations.

While the Kalman-filter was originally aimed to provide an optimal estimator for sequential data assimilation, that is an iteration of analysis and forecast (see e.g. Brasseur and Verron 2006), the statistical assessment of observing networks could use the analysis step only. Here we remind that in the analysis step, the Kalman-filter balances the error statistics of the model with the error statistics of the measuring instrument in order to derive the weights for the corrected forecast. Assessment schemes like the OSE make use of the idea, that the analysis step can be used separately to test real observations for their significance (Oke and Sakov 2008; Le Hénaff et al. 2009). However, this approach required the full statistics of the model and the observations and in principle could only be applied to already completed survey missions. SEON further simplifies the assessment of observing systems allowing the a priori assessment of future surveys (Schulz-Stellenfleth and Stanev 2010; Grayek et al. 2011). In order to achieve this, it does not depart from the error statistics but estimates the quality of a reconstruction based on the model state vector itself (Schulz-Stellenfleth and Stanev 2010; Grayek et al. 2015). Similarly to the OSSE, the SEON can also work with simulated observations (SESON), that is proxy data sampled from the model. In this study the required model statistics was estimated from a single model run. It should be mentioned

that there are alternative approaches based on model ensemble runs (e.g. Evensen 2009).

The data needed for our experiments has been generated by a numerical model of the Ems Estuary. We used the Semi-implicit Cross-scale Hydroscience Integrated System Model (SCHISM) which has been developed on the basis of the Semi-Implicit Eulerian Lagrangian Finite Element Model (Zhang and Baptista 2008). The model area covers part of the southern North Sea next to the Ems mouth, the outer estuary and the tidal river (Fig. 1a). The model forcing uses data from the North-West European Shelf model which is part of MYOcean project. These data include horizontal velocities, sea surface elevation, salinity and temperature at the seaward open boundaries. The model has been thoroughly validated (Pein et al. 2014), who showed that it successfully simulates the salinity dynamics in the estuarine main channel downstream from and including the region of Pogum (Fig. 1b, cf. Fig. 7 in Pein et al. 2014). The quality of these simulations is a prerequisite for the present study. Further refinement of the model grid and validation proved that the model provides realistic results also upstream from Pogum (not shown). The model grid finally consists of 93514 nodes in the horizontal and 26 sigma layers in the vertical direction. Although the model area comprises the tidal river, we regard our results concerning this area as as a coarse representation of the real system given the strong influence of high concentrations of suspended sediments in the region (Winterwerp 2011). For the analyses performed in this study we created a data set of 15 days of salinity data starting from the 5th of June 2012 and ending with the 19th of June 2012 where the temporal resolution equals 20 min.

2.2 Approximation of the state covariance matrix

The background information is derived from the model state X . X consists of n rows and m columns where the columns contain the state at time j and the rows contain the time series at a certain node and level i of the model grid. For the sake of computational efficiency the rank of the proxy data was reduced by

an decomposition into its Empirical Orthogonal Functions (EOF) (Brasseur and Verron 2006, Lermusiaux and Robinson 1999). In the case of the SESON approach, dimension reduction is directly applied to the state vector (Grayek et al. 2015). By means of the decomposition, the data set is represented by a linear combination of its EOFs, *eigenvalues* and Principal Components:

$$X = U\Lambda V^T \quad (1)$$

where the columns of U comprise the *eigenvectors* u , the *eigenvalues* are given by the diagonal of Λ and the principal components v reside in the columns of V^T . The triple of one EOF, *eigenvalue* and PC describes one mode of the temporal variance in the data. A number l of modes approximates X :

$$X^{(l)} = \sum_{k=1}^l u_k \lambda_k v_k^T \quad (2)$$

Several algorithms exist to achieve the decomposition. All algorithms make sure that the EOFs form an orthonormal basis, so that $\langle u_i, u_j \rangle = 1$ for $i = j$, and $\langle u_i, u_j \rangle = 0$ otherwise. By convention, the eigenvalues λ are sorted according to their importance, the first one representing the most of the variance in the data. The covariance matrix, which can be approximated by

$$P \approx U_l \Lambda U_l^T \quad (3)$$

is central to SESON (Grayek et al. 2015), where U_l contains the first l dominant modes as columns. The basic assumption is that the physical system is fully represented by the numerical model and that the background statistics of the model

in the form of the covariance matrix fully determine the spread of information in time and space.

In the framework of our assessment method, P contains the information which is contributed by the model. From the side of the observations the positions of the probes are needed. Given a stationary observing array, the observation operator H has the same dimension as X with $h_i = 1$ in the observation locations and $h_i = 0$ elsewhere.

2.3 Estimation of the Kalman gain and the reconstruction error

As has been emphasized in the introduction to this section, the SESON inherited from the sequential data assimilation the statistical instruments of the so-called analysis step. In this step the real state of the physical system is linearly estimated from the observations:

$$x = Ky \tag{4}$$

where K is the Kalman gain matrix. Here we have assumed that the mean is removed from both the observations and the model state vector. K optimizes the informational gain from an observation assimilated into the observing system (Brasseur and Verron 2006). In the framework of SESON, the Kalman gain assures the estimate of the *posterior* errors to be optimal (Schulz-Stellenfleth and Stanev 2010). In order to derive K from the covariances and the observation operator the classical approach (Kalman 1960) is

$$K = PH^T(HPH^T + R)^{-1} \tag{5}$$

where H is the observation operator, which relates state vectors and observations according to $y = Hx$. R contains the observation error covariances. Usually the observation errors are assumed to be uncorrelated, i.e., R is a diagonal matrix.

Any modelling or observation of the ocean state is subject to errors. In the classical data assimilation the error models contribute to the optimal balance between the model and the observing system. In the framework of SESON model errors do not play the same central role. Instead the model variability is assumed to represent the errors assigned to the synthetic observations (c.f. eq. 5 and eq. 3).

The observation error is composed of an instrumental error and a representation error (Brasseur and Verron 2006, Oke and Sakov 2008). The latter exemplifies the physical scales which are not represented by the model (Oke and Sakov 2008). It also comprises the interpolation error which is associated with interpolating an observation onto the model grid. We assume the instrumental error to be constantly $0.1[psu]$. In order to increase the realism and discriminative power of the assessment procedure, we will additionally take into account a representation error (RE). Here we define the RE as the product of the horizontal variability of salinity and horizontal velocities (cf. Cummings 2006):

$$\epsilon^r = \sqrt{(dS/dx)^2 + (dS/dy)^2} \sqrt{(du/dx)^2 + (dv/dy)^2} T_s \quad (6)$$

where T_s is the sampling period. The RE is added to the instrumental error so that the sum gives R in eq. 5.

Having calculated P, H, R and K it is possible to quantify the reconstruction error standard deviation:

$$\sigma^r = \sqrt{DIAG(P - KHP)} \quad (7)$$

.

The model state vector standard deviation is given by:

$$\sigma_X = \sqrt{DIAG(P)} \quad (8)$$

.

Finally the quality of the reconstruction is characterized by the relative error

$$\sigma_I^{\%} = \frac{100\% * \sigma_I}{\sigma_X} \quad (9)$$

This error is 100% if the observations provide no additional information and 0% if the measurements are perfect.

2.4 Relative explained variance

The assessment of a limited number of observing stations can be logically extended in order to estimate the explained variance by single point measurements. For that purpose the method described in the previous sub-section is applied to every point in the model grid. The so-called relative explained variance of this point is then defined as:

$$\sigma_{\chi}^{\%} = 100\% - \sigma_I^{\%} \quad (10)$$

Mapping the results gives a footprint of the evaluated variable that allows for the identification of the most important dynamical regions of the physical system. In some of the following analysis we will consider spatial averages of $\sigma_{\chi}^{\%}$. This χ is of particular interest for single point measurements, where maps of mean relative explained variance can be produced, which give an indication how valuable observations at certain locations are.

2.5 Assessment of observing networks based on the cross-covariance matrix

To take into account that an observation platform moves in time and space, the proxy data has to account for the spreading of information in both space and time, too. A straightforward mean to achieve this is to augment the covariance matrix

by the cross-covariances between subsequent time steps. For our case this means that the singular value decomposition (eq. 1,2) is applied to an extended state vector of the form

$$\hat{x}(t) = (x(t), x(t - \Delta t), x(t - 2\Delta t), x(t - 3\Delta t), \dots) \quad (11)$$

,
 where Δt equals the time step of the model output. The number of time lags determines the time span covered by the synthetic observations system. For a first try, we set the time lag to the temporal resolution of the model data and we consider a total of five time lags. It follows that the extended state vector contains the cross-covariances between all nodes up to the lag of 100min between the original data and the lagged data. It is then possible to create an extended measurement operator \hat{H} of the same dimensions as \hat{X} that describes the trajectory of the observing system in time and space. Consequently, eq. 5 is modified in the following way (see Schulz-Stellenfleth and Stanev 2010):

$$\hat{K} = \hat{P}\hat{H}^T(\hat{H}\hat{P}\hat{H}^T + R)^{-1} \quad (12)$$

.
 If we follow the procedure given by the eq. 7,8 and 9, we obtain an estimate of the reconstruction error not only for $x(t)$ but also for $x(t - \Delta t), x(t - 2\Delta t), x(t - 3\Delta t), \dots$.

3 Results

3.1 EOFs

Although the EOFs do not necessarily represent distinct physical processes (cf. Sec. 1) they can be linked to one or several dominant dynamical patterns. In any

case they determine the outcome of the SESON (cf. eq. 5) and should therefore be considered in detail.

The first EOFs accounts for more than 60% of the variance in the background data (Fig. 2). It is most prominent in the region of the salinity front (Figs. 3a, 4a). A harmonic analysis of the PCs reveals that the first PC contains most of the energy of the M-2 tide (Fig. 2b). The harmonics of M-4 are almost equally or even stronger represented by the first three PCs. Generally speaking, the first EOF and PC thus describe the tidal intrusion and the back-and-forth oscillation of salinity in the estuary.

In the frequency band below the M-2 frequency a number of spurious peaks can be identified. One of them arises roughly at the period of the diurnal tide. Longer cycles become even more spurious and can be traced back to modulations of the salinity field caused low pressure systems passing through the atmosphere above Ems Estuary (not shown).

The pattern of the second EOF reveals the contours of the freshwater plume (Fig. 3b, cf. 1b). The horizontal pattern connects the baroclinically influenced region of the estuary (Pein et al. 2014) with the shallows along the coast East of Ems estuary. On the other hand, all regions North and West of this “Region of Freshwater Influence” (ROFI) are almost not seen by this EOF. In the along-channel direction this EOF reflects the estuarine salinity gradient (Fig. 4b). Although it is of minor importance compared to the first EOF, this EOF represents about 20% of salinity variance. Consistent with the theoretical understanding, the related PC has its spectral maximum in the frequency band corresponding to the period of the spring-neap cycle.

The third EOF almost mirrors EOF-2 (Fig. 3c). Also in the along-channel direction it is very similar to the second EOF (Fig. 4c). However, EOF-3 “sees” the salinity stratification between km 40 and km 70, which is the region of the salinity front (Pein et al. 2014). Also in the frequency domain (cf. Fig. 2b) PC-3 largely resembles

PC-2. It is important to note that this mode contains only roughly a third of the variance of the second mode and is about one order smaller than the first mode. Higher EOFs cannot be easily associated with the dominant physical processes (Fig. 3d). One could speculate that EOF-4 reflects the tidal salinity front in the river and its connection with the regions surrounding the western tidal inlets and the central Ems Estuary north-west of Knock (Fig. 3d). Its pattern roughly replicates EOF-1 but better 'identifies' areas controlling the salinity front, i.e. the main channel in the outer estuary and the inlet-delta systems between the barrier is-lands. Although they relate to the primary dynamics, these controls show much smaller amplitudes than the tidal river and therefore moved to the subordinated EOFs. PC-4 reveals higher spectral energy at the period of the main lunar tide and its over-tides (Fig. 2b). This supports the interpretation that EOF-4 represents smaller details in tidal variability of the salinity field. From the analysis of the decomposition of the salinity data into its EOFs and PCs it becomes clear that the greatest part of the variability relates to the dominant tidal processes whereas a smaller but non-negligible part represents the sub-tidal baroclinic processes.

3.2 SESON of the complete model area

3.2.1 Stationary profiles of salinity (*Borkum, Knock, Pogum*)

Stationary CTD-devices operated by the Federal Waterways Agency (WSA) permanently observe surface salinity or take vertical salinity profiles along Ems Estuary (Fig. 1a). In order to address the impact of these observations when reconstructing salinity in the entire area, we perform a SESON for each of the three stations in Fig. 1a and for the possible combinations of these stations. For the sake of simplicity we assume that all stations measure the complete salinity profile. The results will be presented below in terms of reconstruction error (see eq. 9)

The first SESON involves a single station at the entrance of tidal river (see for the positioning Fig. 1a). This experiment yields low errors in the vicinity of the instrument whereas farther away the errors exceed 35% in the main channel and 50% elsewhere (Fig. 5a). Moving the single observation platform to Knock considerably improves the overall error (Fig. 5b), illustrating how important the position is to get maximum relevant area-wide information from a single measurement. Some of the major improvements occur relatively far away from the point of observation, around the neighbouring tidal inlets. Not surprisingly, the lowest error estimates are found upstream and downstream from the measuring station. The scope of the reconstruction with an error level lower than 30% (cold colors in 5) corresponds roughly to the tidal excursion of salinity reported for this area (Pein et al. 2014 Fig. 7a). The reconstruction decreases slowly in seaward direction whereas it degrades rapidly towards the tidal river. The mouth of the tidal river seems to 'shield' the spread of information towards the outer estuary even though it is in the reach of tidal excursions from Knock.

The error estimates based on the Borkum station resulted in a slightly different footprint (Fig. 5c). The best reconstruction was found in the estuarine inlet, the tidal delta and the beginning of the estuarine main channel. Again, information does not spread isotropically. In the flood direction the error decreases linearly, increasing steeply only over the channel flanks. In the ebb direction the optimally reconstructable region deflects to the East, i.e. it conforms to the direction of ebb flow under the influence of the Coriolis force. This pattern reveals the delta-like outflow from the ebbing estuary; errors rise sharply towards the open sea.

In the next step we combined the Borkum and Knock stations which led to a much smaller RMS error (Fig. 5d). In addition the error field gained higher contrasts. It clearly isolates the main estuarine channel and the smaller tidal system from the open sea and the tidal river. This drawback reduces when using Knock and Pogum stations instead (Fig. 5e). Also these two stations bring about a smaller overall error which can be attributed to the large variability in the tidal river captured by

Knock station (cf. 3a). Results further enhance when operating all three stations simultaneously (Fig. 5f). The overall error dropped to 52% and it even fell below the 30% mark between the stations. Beyond that, the quality of reconstruction also improved in the open sea, leaving behind certain areas north of the barrier islands and the shallows west of the main estuarine inlet. The correlations between between the dynamics in the estuary and the open sea imply that measurements in the open sea are beneficial when describing the variability in the estuary. A more complete, call it ideal stationary observing system, which covers both the open sea and the estuary (Fig. 1b), dramatically improves the quality of reconstruction.

3.2.2 An ideal stationary observing system

In the following experiments, twelve imaginary CTDs have been placed next to the open boundary, in order to capture the fluctuations caused by the tidal wave travelling along the coast (see the locations indicated by the dots in Fig. 1b). Similarly to the experiments described in the previous section, further imaginary devices were added along the tidal river and Wadden Sea. The devices were placed successively at (1) Pogum, (2) Knock, (3) Dukegat, (4) Borkum, (5) in the back barrier region of Norderney, and (6) in Ems River near Leer (the numbers correspond to the labels next to the crosses in Fig. 1b).

The first experiment in which station (1) was added to the twelve ones north of the barrier islands (cf. Fig. 1b) resulted in an average error of 23.7% (Fig. 6a). Reconstruction excels in the vicinity of the observed locations and in a large region in the North-East of the model area. Reconstruction performed poorly in the region North of the barrier islands. Reconstruction errors were also low over some of the tidal flats, for example in the most Western part of the model area.

The next experiment involved one more station (2) at Knock. As a consequence, the overall error dropped to 20.6% (Fig. 6b). The greatest improvement was achieved in the Knock region, which was the area of lowest reconstruction errors in the single-station experiments (Fig. 5b).

By adding another station (3) at Dukegat (Fig. 6c), the errors decreased not only in the vicinity of the new station but errors reduced in large parts of the main channel and in its tidal delta. This improvement is reflected by the mean error, which dropped to 16.9%. However, the error patterns North of the barrier islands persisted. Actually, the error pattern is similar to the one when only three single stations were part of the observing system, although the mean error is much lower (Fig. 5e). At this point it becomes evident that the sloping region north of the barrier islands is dynamically decoupled from the main physical regimes in the studied area. It clearly separates the open ocean and the estuarine part of the model area.

Complementing the observing system by another station at Borkum (4), the reconstruction errors overall became slightly smaller (Fig. 6d), however no substantial changes of the error patterns were observed. In the last two experiments two extra stations were added in the back barrier region of Norderney (5) and in Ems River (6) near Leer. The former enhanced reconstruction in large parts of the back barrier basin (Fig. 6e). Results made further advances in the tidal inlet of Oosterems and over the tidal flats separating the two inlets of Ems Estuary. In the last experiment reconstruction errors dropped in the tidal river whereas no change took place in the main parts of the model area (Fig. 6f).

This set of experiments proved that the envisaged 'ideal' observing array (cf. Fig. 1b) yields very low errors over large parts of the model area. Nevertheless, some areas could not be reconstructed better than 75% of the observed variance. This applies to the sloping region north of the barrier islands and the back-barrier shallows of Borkum. In reality, a stationary observing system cannot be deployed at a very high density. On the other hand measuring devices like the CTD can be operated on research or other vessels. These would capture small-scale spatial and temporal gradients better than the stationary system. In the next section we will therefore assess the impact of moving observation platform.

3.3 Moving observation platform

In a previous study we validated our numerical model by means of ship-born CTD-measurements taken in the main channel of Ems Estuary (Pein et al. 2014). The survey started at Borkum at high tide and covered the main estuarine channel until Ems storm surge barrier (cf. Fig. 1a), moving against the ebbing tide (Fig. 7a). Such a survey has a high chance to prove the model wrong. If on the other hand it successfully validates the simulation, the realism is proved for a representative part of the dynamics in the time-space plane. The question arises however, to which degree this validation strategy captures the dynamics beyond the locations where samples have been taken. In the following we therefore quantify the reconstruction error given a dynamical representation of the observation operator and of the proxy data.

As described in Section 2.2 we tackle this task by allowing the covariance matrix P to comprise in addition to the spatial covariances also the temporal cross-covariances. The dynamical interval represented by this extended covariance matrix equals the time difference between the state vector at the original time and the state vector at the maximum time lag $t - l\Delta t$, where $\Delta t = 20min$ and $l = 5$ in our case. Consequently, \hat{H} contains the trajectory of the observing system for the same time interval. Since our survey took longer than the time span covered by \hat{P} we simply performed the analysis for a moving time window, with each part covering a different section of the complete transect (see the dashed lines in each sub-figure of Fig. 8).

To start with, we hypothesised the observations along the transect to be constant in time using the simple covariance matrix (Fig. 7a). Such a configuration leads to an error pattern resembling the three-stations experiment (Fig. 5f) but with a significantly smaller overall error. Adopting the new concept of considering temporal cross-covariances, the overall quality of reconstruction improved significantly (Fig. 8 with different colorbar than Fig. 7c). The biggest changes occurred in the sloping region north of the barrier islands although this area is not crossed by the

ship transect. It follows, that the reduction of the errors was achieved due to the modification of the statistical representation of the model dynamics. Here we want to remind, that in principle no new information was used but the statistics were altered in a simple way. In fact the cross-covariances cover only a small time interval ($100min$). It seems that this interval sufficiently captures the more complex dynamics which occur in some regions of the model area.

However as each time slice covered a different region of the channel (Fig. 8a-f), the error fields themselves are subject to further and more detailed evolution. In the first experiment (see numbers Tab. 1) the system achieved a very good reconstruction of the inlet area and the open sea, with errors smaller than 1.5% (Fig. 8a). The same applies to the inlets and to the basins surrounding the main estuarine channel. Outside of the deep water, the shallows and the upstream estuary were reconstructed at error levels equal to the overall RMS error (4.0% see Tab. 1). East of the transect line the pattern clearly reveals the contours of the freshwater plume. Obviously the signal perceived by this observing system cannot easily penetrate the baroclinically influenced areas from the outside. Much higher error estimates can be found in the tidal river.

With the ship transect covering the central outer estuary, the overall quality of the reconstruction increases (cf. Tab. 1). From this position the observing system attains good knowledge not only about the direct environment but “sees” into the neighbouring tidal basins and inlets (Fig. 8b-d). With the transect approaching the tidal river the overall error stays more or less constant. Apparently the gain of quality of reconstruction in the entrance of the tidal river compensates for the deterioration of the reconstruction in the open sea and around the tidal basins (Fig. 8e,f).

Similar to what has been found when simulating the reconstruction error with individual stations (see Sec. 3.2.1), the different regions are separated by a sharp transition from very low to significantly higher errors. Throughout this row of experiments, the tidal river remained the only region with errors almost constantly

higher than 10%, mostly above 15%. Even when the transect entered the tidal river, the reconstruction improved only in the neighbourhood of the trajectory. One conclusion from these experiments is that the tidal river and the outer estuary with the open sea are statistically and dynamically separated. This means that even the extended covariance matrix does not fully capture the degree of complexity of coupling between the two systems.

In the next series of experiments we introduced a representation error (RE) (cf. Sec. 2.3) in order to account for the subscale processes which are not represented by our simulated observing network (Fig. 7b). The variance of this error can mainly be attributed to the influence of the bathymetry on local fluctuations of the horizontal velocities and salinity (see the bathymetric profile in Fig. 4; see also Pein et al. 2014 Fig. 8b). The introduction of the RE in general led to lower reconstruction errors (Tab. 1). Also the overall variability of the reconstruction errors decreased which is illustrated by the reduced contrast of the error field. From the viewpoint of possible relevance of presented results to data assimilation the combination of cross-covariance matrix and RE led to the most promising results. The smoothness of the error fields on the other hand hampers the distinction between physically representative regions and those which are decoupled from the general dynamics.

| Exp.Nr. | 1 | 2 | 3 | 4 | 5 | 6 | 7 | 8 | 9 | total mean |
|----------------------------|-----|-----|-----|-----|-----|-----|-----|-----|-----|------------|
| with constant error | | | | | | | | | | |
| mean | 4.0 | 5.3 | 5.5 | 4.9 | 4.3 | 5.1 | 4.3 | 4.5 | 4.8 | 4.8 |
| standard dev. | 9.3 | 9.9 | 9.5 | 9.0 | 8.6 | 8.5 | 7.3 | 7.0 | 7.2 | 8.5 |
| with varying error | | | | | | | | | | |
| mean | 2.2 | 2.7 | 2.5 | 2.5 | 2.2 | 2.7 | 2.1 | 2.2 | 2.6 | 2.4 |
| standard dev. | 5.7 | 6.0 | 4.4 | 5.2 | 5.1 | 5.0 | 4.2 | 3.8 | 4.2 | 4.9 |

Table 1: The mean RMS error [%] and standard deviation [%] of the SESON with moving observation platform for (top) constant error and (bottom) spatially varying error (see Fig. 7b).

3.4 Domain separation

In the previous sub-section we stated that the tidal river was statistically and dynamically decoupled from the rest of the model area. To be sure about the reliability of our results and in particular of whether the regional difference of the spatial density of the model grid points affects the estimates, we reproduced the EOF decomposition of the data set of simulated salinity interpolated on a 400m structured grid. The resulting EOFs and *spectrum* only slightly differed from the decomposition of the unstructured data (cf. Figs. 2, 3). Therefore it seems natural to analyse the two regions separately in order to increase the contrast when extracting the physical processes in these areas. In the remainder of this paper, we repeat the EOF decomposition for both regions separately and then proceed to a statistical evaluation of the footprint of the nodes of the model grid for all the three decompositions, respectively.

The first four EOFs of the outer estuary and open sea excluding from data processing the tidal river duplicate to some degree the patterns found in the analysis of the whole Ems Estuary (compare Fig. 9a-d with Fig. 3). However, some features seem to have “leaked” from a less important to a more important EOF. For example, the first EOF not only “sees” the tidal salinity intrusion but also the ROFI (Fig. 9a) which in the analysis of the complete model area was a major trait of EOF-2. This EOF overall shows the same dominant patterns as its counterpart in the previous analysis (cf. Fig. 3b). In the north-eastern part of the model area values decay widely so that this area separates from the remainder of the open sea. This area was particularly well reconstructed in the SESONs with fixed stations (cf. Fig. 5) and was reflected by EOF-4 and EOF-5 in the analysis of the whole model area (cf. Fig. 3).

Also the *eigenvalue* spectrum changed (Fig. 9e). The first mode has lost some of its importance, representing merely 50% of the variance in the data set. This seems natural since most of the tidal energy of the salinity signal was concentrated in the tidal river (cf. Fig. 3a). The second mode has the same overall importance as in the

analysis of the complete model area (cf. Sec. 3.1) and thus increases its relative in comparison with the first mode. By excluding the tidal river from the EOF analysis, the baroclinic processes obviously gained more statistical influence. This impression is supported by the harmonic spectrum of the PCs (Fig. 9f). Although most of the variance still resides in the band of the M-2 tide, both M-4 and even more so the spring-neap cycle have gained more importance. The spring-neap cycle is particularly reflected by PC-2 and PC-4. A separate EOF decomposition of the salinity dynamics in the tidal river revealed the dominance of the harmonic processes in this region (Fig. 10). The spring-neap cycle can hardly be distinguished from the spurious oscillations at frequencies lower than M-2. Given the absence of a mode dominated by baroclinic processes more than 90% of the variance are accounted for by the first mode which is mainly represented by the M-2 tide. The second and third EOF reflect the dissipation of the dominant tidal energy to smaller scales. Overall, the tidal river behaves similar to an idealised case of a tidal environment. The domain separation increases the signal-noise-ratio of the dominant physical processes which are in both areas the M-2 tide and its over tides and in the outer estuary and open sea the baroclinical processes controlled by the spring-neap cycle.

3.5 Footprints of salinity

The same framework which we have applied in the previous sections, may be used to give an estimate of the importance of a point or region for the rest of the model area (Grayek et al. 2015). To achieve this, a SESON is performed separately on each node and the relative explained variance by this node is quantified (eq. 10). In the following we report the results obtained from the analysis of (1) entire model area, (2) the outer estuary and open sea, and the tidal river, separately. The analysis of complete model area led to a rather patchy distribution of the explained variance (Fig. 11a,b). Both the surface and the bottom layer “see” the Eastern part of the bay situated between Knock and Pogum and the tidal river

as the most informative region in terms of variance explained. The basic impression is that this footprint combines the most prominent features of the first and second EOF (eg. Fig. 3a,b). Although the differences between the surface salinity and the in bottom layer are minimal in the estuary, the high levels of relative explained variance, in the North-Eastern part of the model area are found only at the surface(Fig. 11b). In comparison the bottom layer lacks contrast and does not discriminate areas eminently beneficial for reconstruction(Fig. 11a). On the other hand it clearly delineates the areas that almost totally decouple from the overall dynamics, .i.e. the slope north of the barrier islands and the crescent-like pattern in the north-western part of the open sea(Fig. 11a).

The exclusion of the tidal river from the analysis resulted in a much higher overall explained variance on the one hand, and higher contrasts on the other hand (Fig. 11c,d). Three coherent regions of about 20% explained variance can be identified. The largest one roughly conforms to the decayed area in the north-eastern part of the open sea which we have found in the EOF-2, EOF-4 (Figs. 3b,d; 9b) and in some of the SESONs described in the previous sub-sections (Figs. 5e; 6). The second largest one conforms roughly to the contours of the ROFI (Figs. 3b; 9b). It demonstrates the great importance of the back barrier region South of Juist and Norderney for the overall salinity dynamics. Although the surface and bottom pattern are mostly in agreement, the tidal delta between Juist and Norderney is visible only at the surface. In contrast, the off-shore regime with low values of explained variance extends into the tidal basin at the bottom. This difference between the top and bottom layer (stratification) exemplifies the far-reaching influence of the freshwater source in the Ems Estuary.

The southern region that proved a powerful indicator for the overall salinity variability is part of Dollart Bay. In one of the simple experiments we have shown this area to be dynamically connected with Knock and the main estuarine channel nearby (Fig. 5b). The explained variance pattern reflects this connection. The high values of explained variance emerge in the direction of the ROFI downstream, only

to be interrupted by the back barrier shallows South-East of Borkum (Fig. 11d). This underlines the role of these shallows which divide the flood-originated waters on its western side from the baroclinically-influenced waters on its eastern side. The efficiency of this divide in decoupling the different regions changes with the spring-neap-cycle (cf. Fig. 2b). As in the previous analyses, two regions of low statistical impact stand out, both at the bottom and at the surface. These are the sloping region north of the barrier islands and the adjunct half-circle isolating the north-west of the model area from the rest. The analysis of the tidal river only revealed a zone of high explained variance in the central part of the basin (11e,f). Values of $\sigma_{\chi}^{\%}$ decrease smoothly towards the boundaries of the tidal river. It seems that the transition between the outer estuary and the tidal river modulates the salinity signal such that this area slightly decouples from the overall dynamics of the basin. By coincidence, the pattern of $\sigma_{\chi}^{\%}$ in the tidal river roughly conforms to the estuarine turbidity maximum (Talke et al. 2009).

3.6 Physical interpretation of the results

From the above set of experiments it became clear that large parts of the Ems region interact with one another. Given 15 or more well distributed permanent measuring stations, the salinity state vector can be reconstructed up to 88% of the total variance (Fig. 6f). However, the pattern remained patchy and broken by zones of ever-high errors. The full analysis of every grid point against the whole grid (Sec. 3.5) revealed two regions in the open sea which remain inaccessible for the covariance-based reconstruction (Fig. 11c,d). One area is the slope North of the barrier islands with the exception of the tidal delta of the main estuarine channel. The other area extends North of the main tidal delta towards the northern open boundary, forming a broad stripe that separates the waters of the north-western

model area from the waters north of Juist and Norderney islands. Which physical processes could explain the high reconstruction errors in these two regions?

In the following we examine the salinity dynamics along the meridionally and zonally oriented transect lines in Fig. 1b. The tidally-averaged salinity reveals a well-mixed region around km 20-30 of the meridionally oriented transect (Fig. 12a). In the southern direction stratification increases and the average explained variance of this region is as high as 8% (Fig. 11c,d). In the northern direction vertical salinity gradients become slightly greater with depth but the representativeness approximates zero.

The area of weak stratification can be identified along the zonally oriented transect line between km 20 and km 30 (Fig. 12b). However, stratification does not necessarily decouple a region from the overall dynamics, since another stratified region between km 50 and km 60 proves to be highly representative for the whole model area. Firstly, the latter area strongly responds to the spring-neap-cycle (Fig. 12c). The great role of the spring-neap cycle seems to be confirmed by the pattern of the ratio between mean spring and mean neap surface salinity (Fig. 12c) which reveals the contours of the regions of high explained variance represented in Sec. 3.5. We remind here that the spring-neap-cycle makes up a significant part of the variability represented by the more important EOFs (cf. Sec. 3.1). Similar distinctions between the eastern and western part of the open sea can be made concerning other tidal constituents (Fig. 13e-h). Between km 50 and km 60 the amplitude of the M-2 and M-4 tides are relatively small. Between km 40 and km 50 only the M-2 constituent exceeds an amplitude of 0.5 PSU and drops to zero near km 40. West of km 35 both M-2 and M-4 tides become relatively strong. At the same time the phase relation between the two constituents changes drastically. This configuration of the tidal harmonics leads to a strong modulation of the M-2 tidal signal exactly in the region which was found to decouple from the overall dynamics. On the border between the two regimes, the phases of the M-2 component differ by roughly half a tidal cycle which reduces the tidal amplitude to almost

zero. Such a behaviour cannot be captured by the simple covariance matrix (eq. 3). Coming back to the meridional transect line, a similar border separating the estuarine dynamics from the open sea can be spotted around km 20 (Fig. 13a-d). The area where the two transect lines cross is surrounded by interfaces of opposing tidal regimes. That is why the reconstruction largely failed in this region (cf. Fig. 11c,d). Possibly the north-western model area receives additional forcing from the Rhine ROFI (de Boer et al. 2009). This would imply that the salinity dynamics in the area feature a higher degree of stochastic variance that is not connected to Ems River.

As we have demonstrated in Sec. 3.3, the use of the temporal cross-covariance information overcomes the difficulties associated with the non-linear dynamics. For the understanding of the inner correlation structure of the model area it was very fruitful to reconstruct the state based on the simple covariance matrix.

4 Discussion

In the framework of data assimilation, the reconstruction error of a specific observing network is quantified with the help of OSE or OSSE. The latter has been criticised to lack realism, since other than the OSE, in the OSSE the model simply assimilates data produced by itself (Arnold and Dey 1986). That is why it was proposed to move from the so-called identical-twin experiments to the fraternal-twin experiments, i.e. experiments in which the simulated observations were sampled from a different model (Halliwell et al. 2014; Williamson 1973; Williamson and Kasahara 1971). Alternatively, the real observations could be substituted by dummy observations from another source (Ballabrera-Poy et al. 2007). In order to insure the realism of the OSSE, authors modified the identical-twin experiment by adding white noise to the simulated observations (Arnold and Dey 1986). The above objection brought forth against the identical-twin OSSE could be addressed towards a number of studies including this one which assess the impact of an observing network recurring to a purely statistical assimilation simulation (Schiller

et al. 2004, Le Hénaff et al. 2009, Ngodock et al. 2006). They have in common to rather mimic an OSSE by comparing the variance represented by the sampled observations to the overall variance in the proxy data. Here we want to remind that these methods do not claim to fully represent an assimilation experiment. Still the approach is able to compare how different observation networks constrain the degrees of freedom of the model state errors (Le Hénaff et al. 2009). In doing so, the SESON and related methods achieve one of the basic objectives of the OSE and OSSE which consists in finding the observing array configuration that best captures the model error structure (Ballabrera-Poy et al. 2007). In this study we have demonstrated that the inner correlation structure of the model covariances reflects the physical processes governing salinity dynamics. From the above results it became very clear which regions and processes can be dealt with by a linear approach and which regions and processes will remain undetected by the traditional methods. In the Ems region SESON framework thus fulfils our objective to identify the necessary and optimal observation locations and density of observations to be able to reconstruct the system state.

In the context of data assimilation the state reconstruction can be hampered by high noise level in the covariances (Hamill et al. 2001). Naturally, correlations are high between neighboring regions and decreases with distance. This was actually the reason, why we performed separate analysis of the physically very different regions of the outer estuary and open sea on the one hand, and the tidal river on the other hand. In the literature (e.g. Houtekamer and Mitchell 1998) several filters have been proposed which increase the SNR of the covariances with the help of the localization technique (Hamill et al. 2001). The filter is biased towards near observations while fading out far away measurements. Our approach to tackle the reconstruction from the observations of a moving platform led to an extended covariance matrix which included the cross-covariances for a given time lag (cf. Sec. 3.3). The results obtained with the cross-covariances were much better than with the simple covariances. Here we want to point out that the cross-covariances have

an effect similar to the localization technique. The cross-covariance is the greatest 1) between the signal in a location and the augmented state in the same location, i.e. the auto-cross-covariance and 2) between the non-lagged signal in one location and the lagged signal of the upstream or downstream neighbour. The latter accounts for the physical propagation of the signal. In effect the method increases the SNR in the reconstruction matrix because it better reflects the physical processes in the ocean. Even the non-linearities which arise on the borders between different physical regimes (cf. Sec. 3.6) are well reconstructed. Meanwhile the data basis X has been the same with the covariance information enhanced by the temporal cross-covariances.

5 Conclusions

Stationary observing networks and a moving observation platform have been assessed in terms of their impact on state reconstruction. In these experiments, spatial coverage proved to be an important factor. However, more important than density of observations turned out to be the location of the observations. The evaluations helped to identify three regions to be most representative for the salinity dynamics in the Ems region: the channel near Knock and the southern part of Dollart Bay, the eastern back-barrier region or ROFI, and the eastern part of the open sea (Fig 11c,d). These regions were shown to strongly respond to the spring-neap cycle. In contrast, the quality of the reconstruction was reduced in areas 1) where the response to the tidal cycles was weaker, 2) where the phase of the main lunar tide changed abruptly and 3) where strong over-tide generation occurred. The overall conclusion is that the spring-neap cycle increases the linearity of the signal which in turn leads to a good representation of the signal by the covariance matrix. The more difficult to reconstruct regions or less linear regimes could be tackled by introducing the temporal cross-covariances to the background statistics. In this case the errors were much smaller even when only part of the original transect was used for reconstruction. The temporal cross-covariances give an ex-

cellent representation of the correlations between neighboring locations. They do so without making use of a localization technique.

6 Acknowledgements

We want to thank Joseph Zhang (VIMS, USA) for his support of our work with the SCHISM model. We also want to thank Thomas Badewien (ICBM, Germany) for providing the data used in this study.

References

- Arnold, J., Dey, C.H., 1986. Observing-systems simulation experiments: Past, present, and future. *Bulletin of the American Meteorological Society* 67, 687–695.
- Ballabrera-Poy, J., Hackert, E., Murtugudde, R., Busalacchi, A.J., 2007. An observing system simulation experiment for an optimal moored instrument array in the tropical indian ocean. *Journal of Climate* 20, 3284–3299.
- de Boer, G.J., Pietrzak, J.D., Winterwerp, J.C., 2009. Sst observations of upwelling induced by tidal straining in the rhine rofi. *Continental Shelf Research* 29, 263–277.
- Brasseur, P., Verron, J., 2006. The seek filter method for data assimilation in oceanography: a synthesis. *Ocean Dynamics* 56, 650–661.
- Cummings, J.A., 2006. Operational multivariate ocean data assimilation. Technical Report. DTIC Document.
- Evensen, G., 2009. *Data assimilation: the ensemble Kalman filter*. Springer Science & Business Media.
- Grayek, S., Schulz-Stellenfleth, J., Stanev, E., 2015. Assessment of the black sea observing system. a focus on 2005-2012 argo campains. *Ocean Dynamics* 99, 999–9999.
- Grayek, S., Staneva, J., Schulz-Stellenfleth, J., Petersen, W., Stanev, E.V., 2011. Use of ferrybox surface temperature and salinity measurements to improve model based state estimates for the german bight. *Journal of Marine Systems* 88, 45–59.
- Halliwell, G., Srinivasan, A., Kourafalou, V., Yang, H., Willey, D., Le Hénaff, M., Atlas, R., 2014. Rigorous evaluation of a fraternal twin ocean osse system for the open gulf of mexico. *Journal of Atmospheric and Oceanic Technology* 31, 105–130.
- Hamill, T.M., Whitaker, J.S., Snyder, C., 2001. Distance-dependent filtering of background error covariance estimates in an ensemble kalman filter. *Monthly Weather Review* 129, 2776–2790.
- Houtekamer, P.L., Mitchell, H.L., 1998. Data assimilation using an ensemble kalman filter technique. *Monthly Weather Review* 126, 796–811.
- Huijts, K., Schuttelaars, H., De Swart, H., Valle-Levinson, A., 2006. Lateral entrainment of sediment in tidal estuaries: An idealized model study. *Journal of Geophysical Research: Oceans* (1978–2012) 111.
- Kalman, R.E., 1960. A new approach to linear filtering and prediction problems. *Journal of Fluids Engineering* 82, 35–45.
- Le Hénaff, M., De Mey, P., Marsaleix, P., 2009. Assessment of observational networks with the representer matrix spectra method—application to a 3d coastal model of the bay of biscay. *Ocean Dynamics* 59, 3–20.
- Lermusiaux, P.F., Robinson, A., 1999. Data assimilation via error subspace statistical estimation. part i: Theory and schemes. *Monthly Weather Review* 127, 1385–1407.
- Ngodock, H.E., Jacobs, G.A., Chen, M., 2006. The representer method, the ensemble kalman filter and the ensemble kalman smoother: A comparison study using a nonlinear reduced gravity ocean model. *Ocean Modelling* 12, 378–400.
- Oke, P.R., Sakov, P., 2008. Representation error of oceanic observations for data assimilation. *Journal of Atmospheric and Oceanic Technology* 25, 1004–1017.

- Pein, J.U., Stanev, E.V., Zhang, Y.J., 2014. The tidal asymmetries and residual flows in ems estuary. *Ocean Dynamics* 64, 1719–1741.
- Schiller, A., Wijffels, S., Meyers, G., 2004. Design requirements for an argo float array in the indian ocean inferred from observing system simulation experiments. *Journal of Atmospheric and Oceanic technology* 21, 1598–1620.
- Schulz-Stellenfleth, J., Stanev, E., 2010. Statistical assessment of ocean observing networks—a study of water level measurements in the german bight. *Ocean modelling* 33, 270–282.
- Talke, S.A., de Swart, H.E., Schuttelaars, H., 2009. Feedback between residual circulations and sediment distribution in highly turbid estuaries: an analytical model. *Continental Shelf Research* 29, 119–135.
- Tranchant, B., Testut, C.E., Renault, L., Ferry, N., Birol, F., Brasseur, P., 2008. Expected impact of the future smos and aquarius ocean surface salinity missions in the mercator ocean operational systems: New perspectives to monitor ocean circulation. *Remote Sensing of Environment* 112, 1476–1487.
- Williamson, D., Kasahara, A., 1971. Adaptation of meteorological variables forced by updating. *Journal of the Atmospheric Sciences* 28, 1313–1324.
- Williamson, D.L., 1973. The effect of forecast error accumulation on four-dimensional data assimilation. *Journal of the Atmospheric Sciences* 30, 537–543.
- Winterwerp, J.C., 2011. Fine sediment transport by tidal asymmetry in the high-concentrated ems river: indications for a regime shift in response to channel deepening. *Ocean Dynamics* 61, 203–215.
- Zhang, Y., Baptista, A.M., 2008. Selfe: a semi-implicit eulerian–lagrangian finite-element model for cross-scale ocean circulation. *Ocean modelling* 21, 71–96.

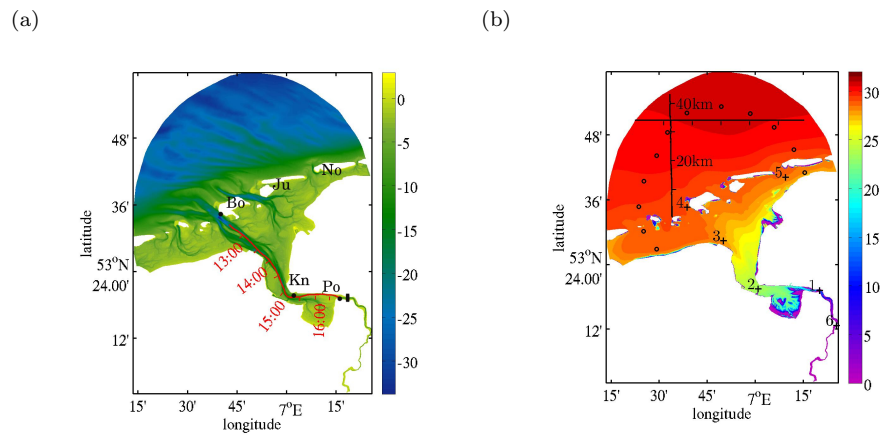
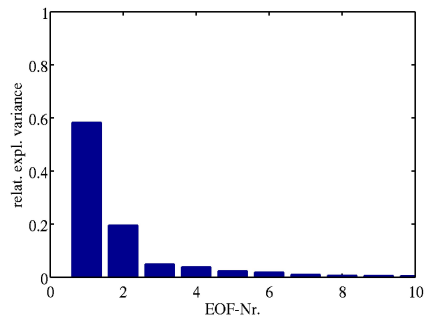


Fig. 1: (a) the model area with the depth [m] as a background. The names of the major barrier islands Ju-Juist, No-Norderney and the three gauges Bo-Borkum, Kn-Knock and Po-Pogum are also given. The red transect line illustrates a ship survey which has been assessed in this study. A small bar next to Pogum indicates the position of the Ems storm surge barrier. (b) the vertically and time-averaged salinity field [psu] which has been derived from 14 days of model salinity data. The dots and crosses represent a hypothetical observing network to be evaluated in this study, where the numbers stand for different experiments. The black transect lines will serve for physical analysis in this paper. Two important geographical locations mentioned in the text are the Osterems inlet which is located between the islands of Borkum and Juist in (a) and a channel section called Dukegat which is indicated by the cross labeled '3' in (b).

(a)



(b)

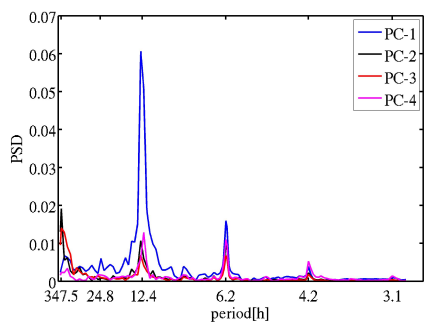


Fig. 2: (a) The normalized *eigenvalues* from an EOF-analysis of 14 days of model salinity output. (b) The power spectral density of the PCs to the EOFs in (a). The EOF decomposition is based on model outputs that cover the period from the 6th of June 2012 until the 20th of June 2012.

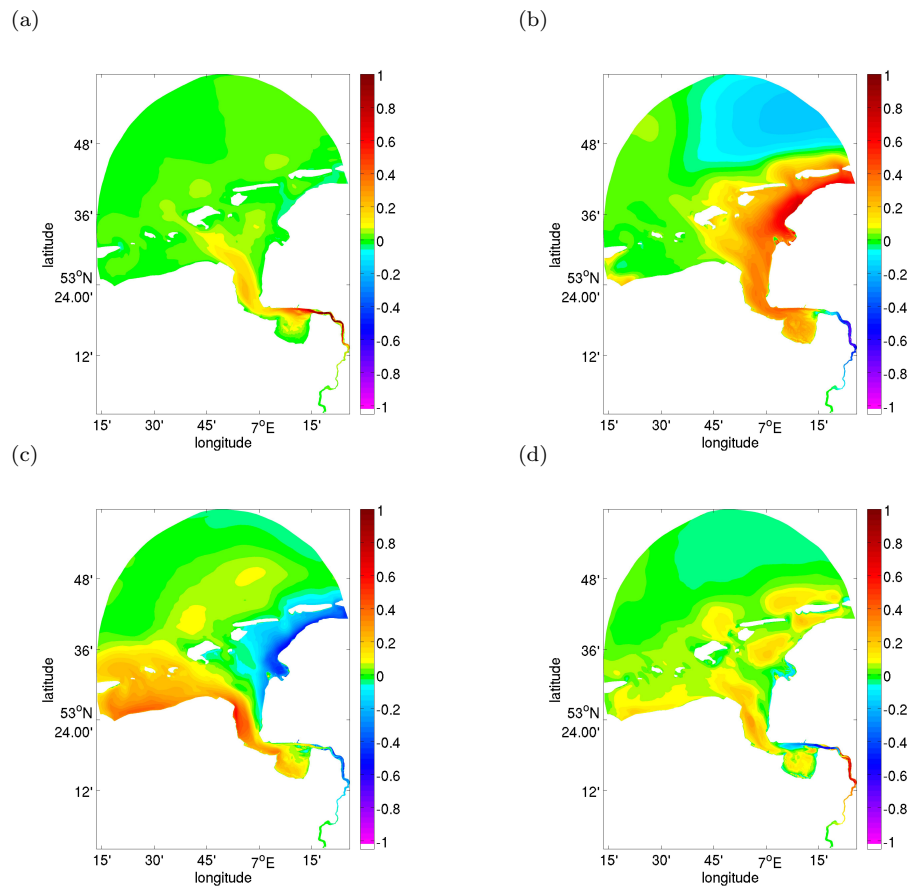


Fig. 3: The empirical orthogonal functions (EOF) one (a), two (b), three (c) and four (d) of the 3D salinity field at the sea surface. The analysis was applied to one spring-neap cycle of data starting from the 2nd June 2012.

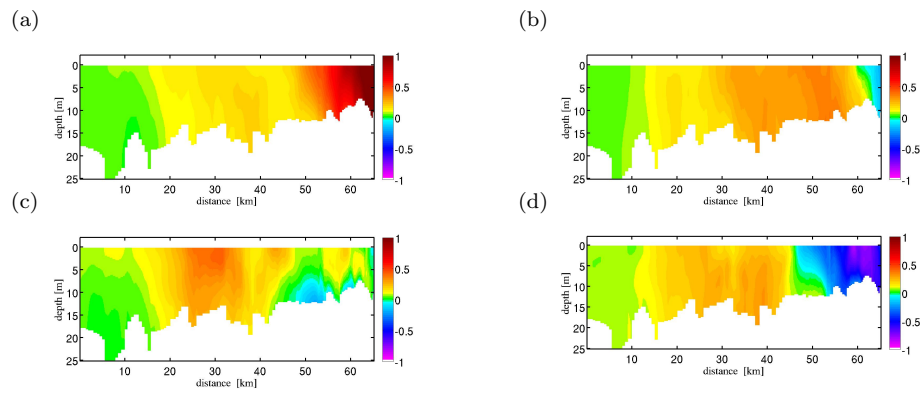


Fig. 4: Along-channel profiles of the four most dominant EOF shown in Fig. 3.

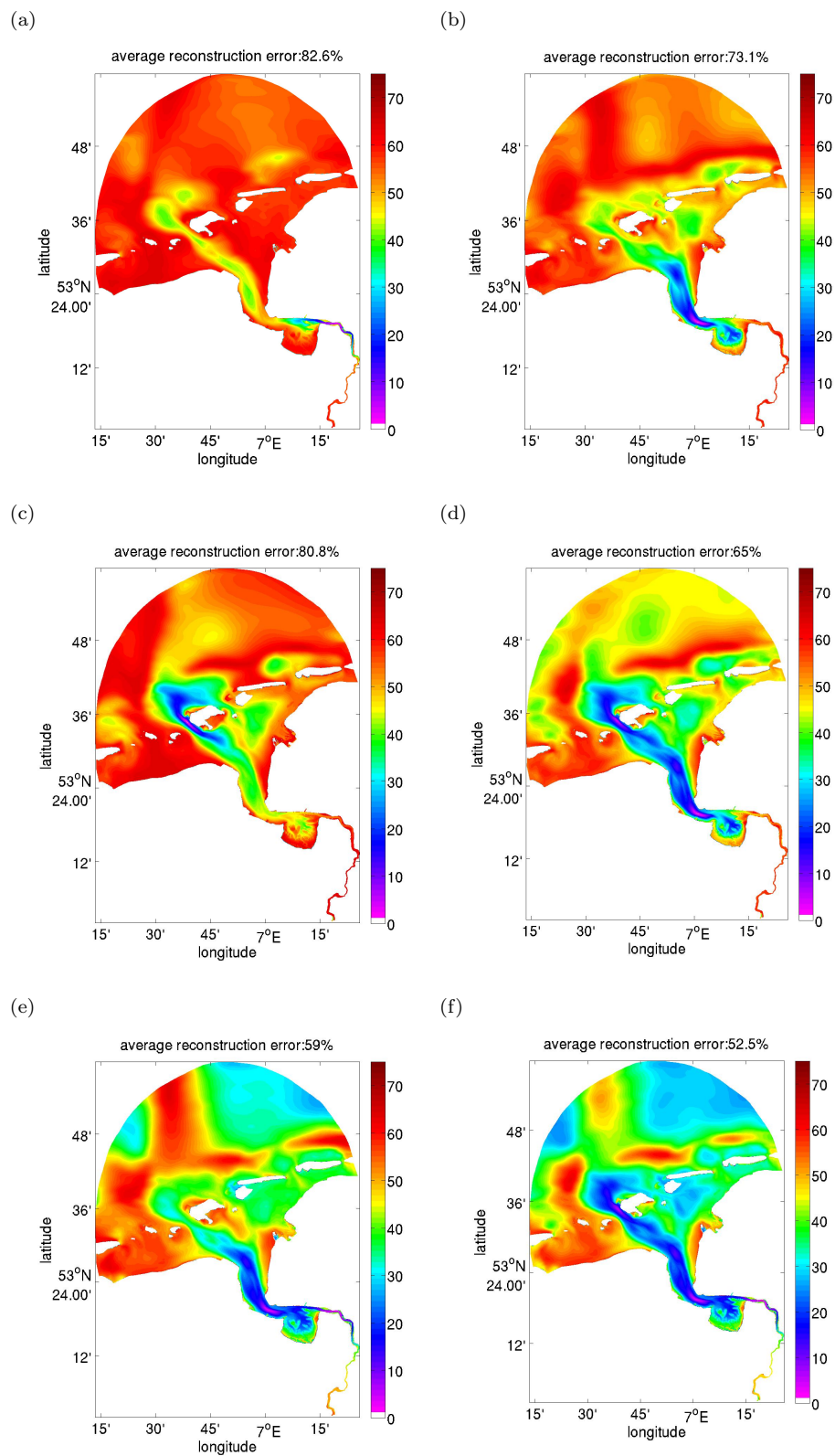


Fig. 5: Reconstruction error fields at the sea surface as obtained from SESONs for (a) Pogum station, (b) Knock station, (c) Borkum station, (d) Borkum and Knock stations simultaneously, (e) Pogum and Knock stations simultaneously, (f) the three stations simultaneously. For the position of the locations see Fig. 1a.

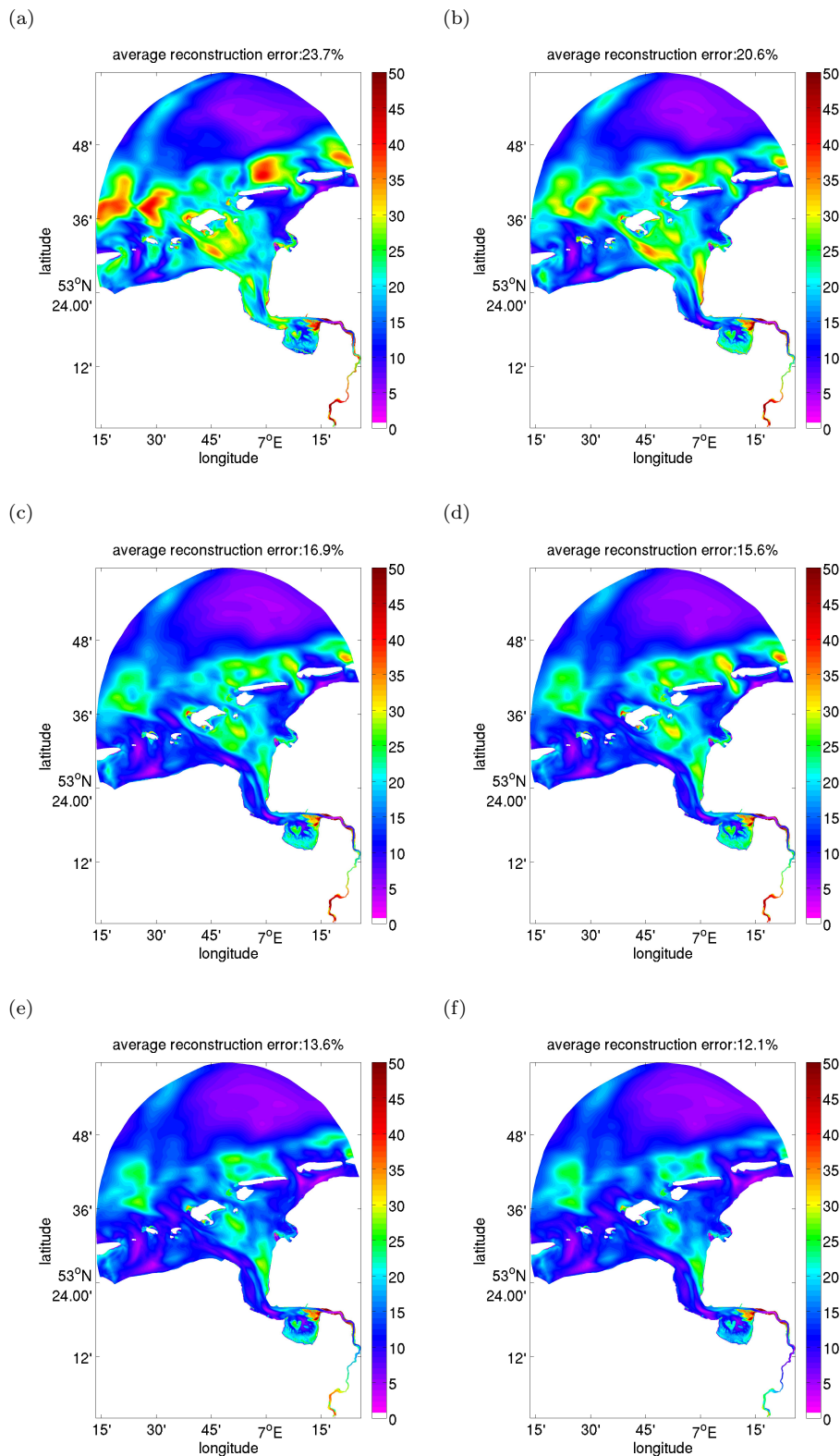
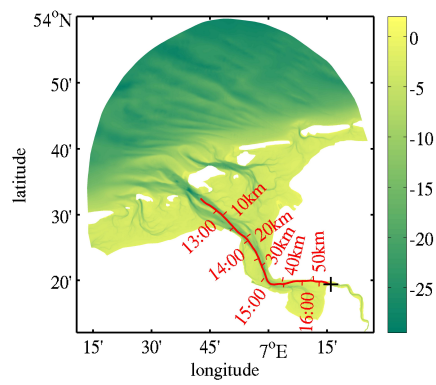
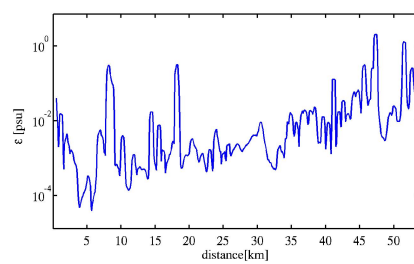


Fig. 6: Reconstruction error fields from the SESONs described in the text (a – Exp.-No. 1, b – Exp.-No. 2, c – Exp.-No. 3, d – Exp.-No. 4, e – Exp.-No. 5, f – Exp.-No. 6). For the position of the locations see Fig. 1b.

(a)



(b)



(c)

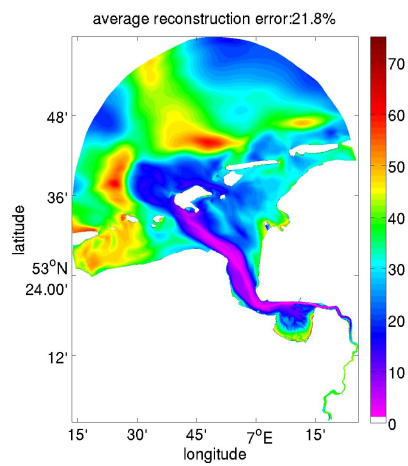


Fig. 7: (a) Ship track along which observations of sea surface salinity and horizontal velocities have been taken with the bathymetry [m] given as a background, (b) Representation error along the transect in (a). (c) Reconstruction error associated with the transect locations taken as stationary observing network.

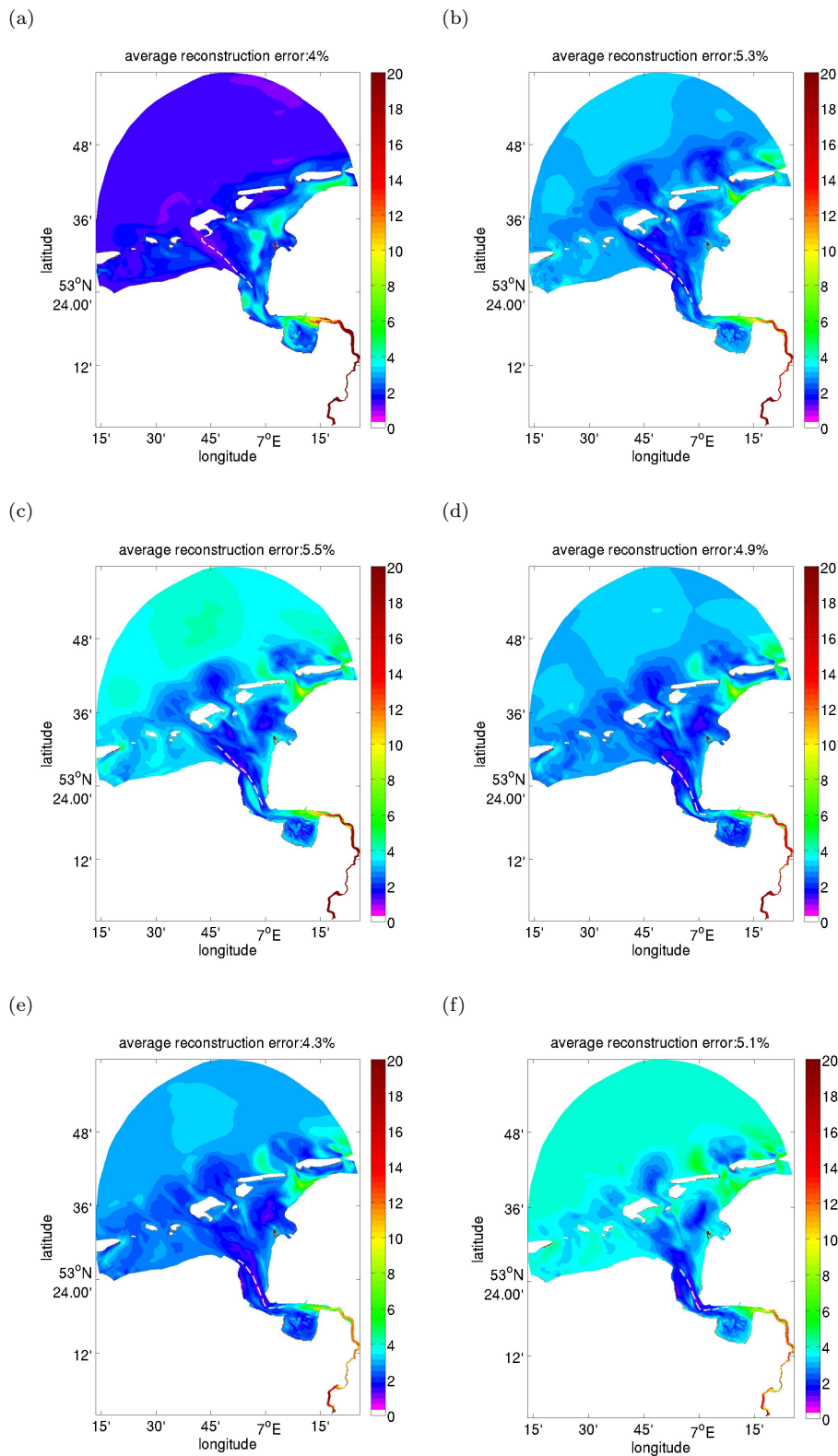


Fig. 8: Reconstruction error fields from the SESONs with an imaginary moving observation platform travelling towards the tidal wave. The transect covered by the analysis is also illustrated (dashed line of light grey color).

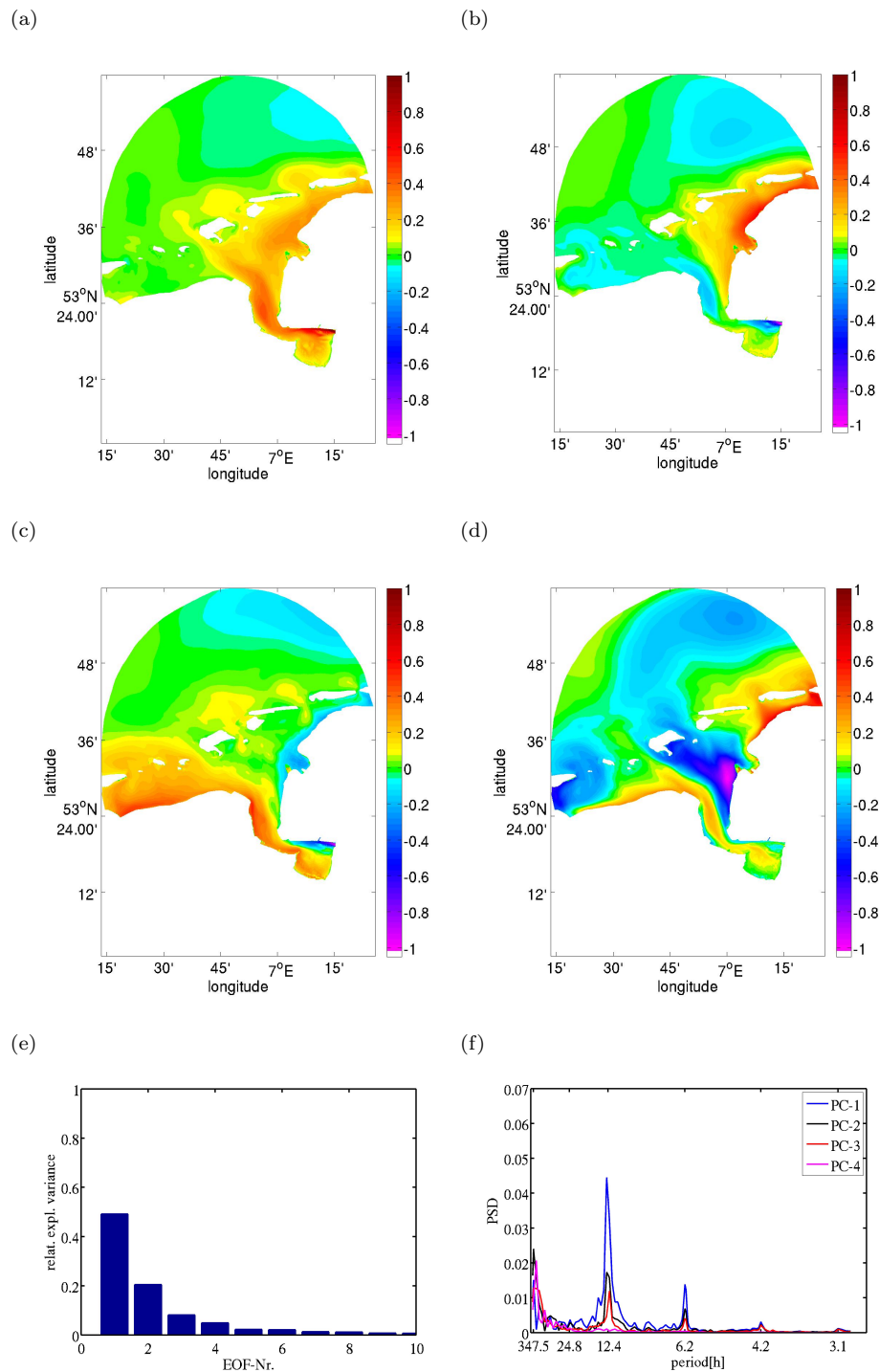


Fig. 9: EOFs one (a), two (b), three (c) and four (d) of the model area without the tidal river. The the *eigenvalue* spectrum (e) and the related principal components (f) are also given.

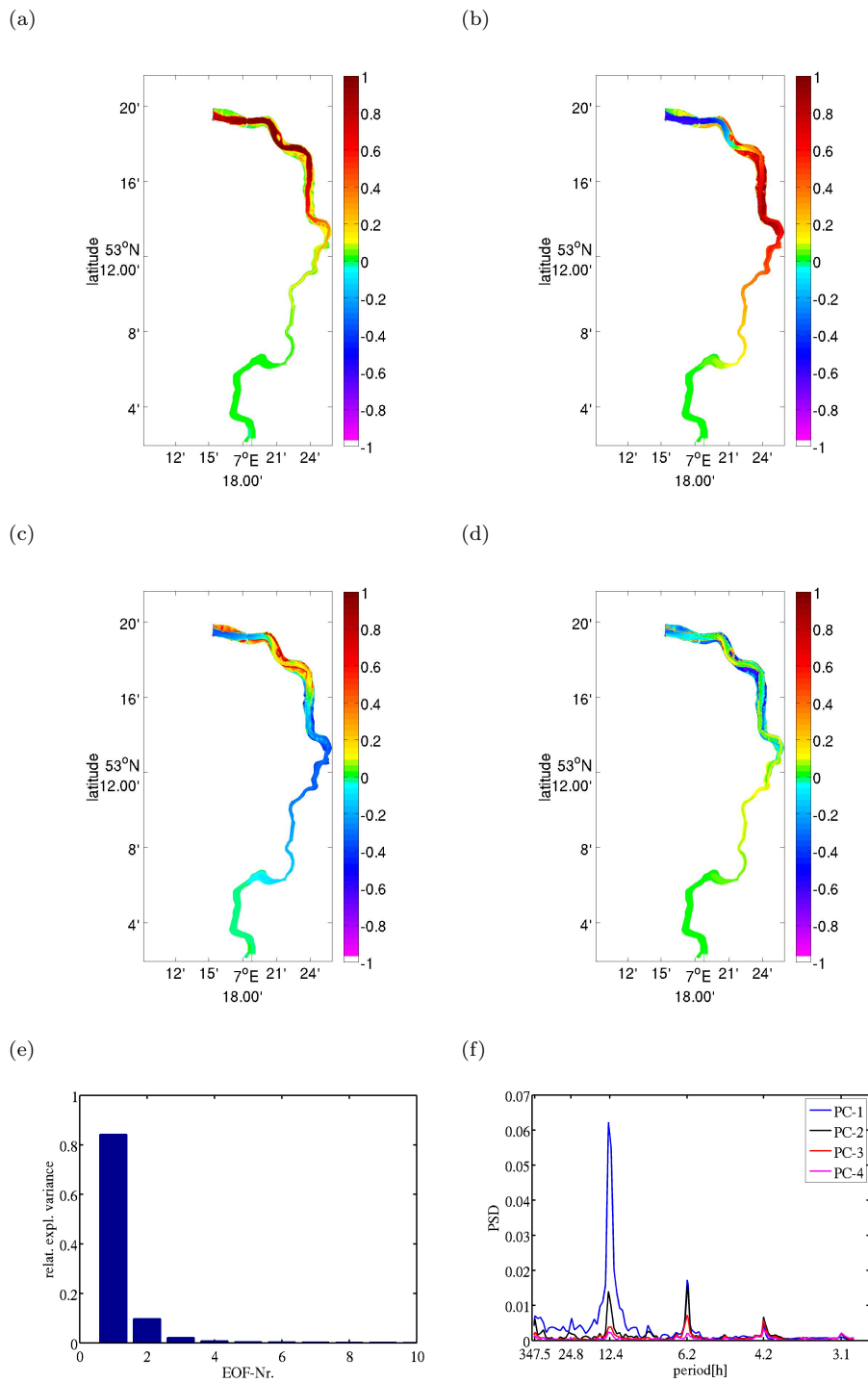


Fig. 10: EOFs one (a), two (b), three (c) and four (d) of the tidal river. The the *eigenvalue* spectrum (e) and the harmonic spectrum of the principal components (f) are also given.

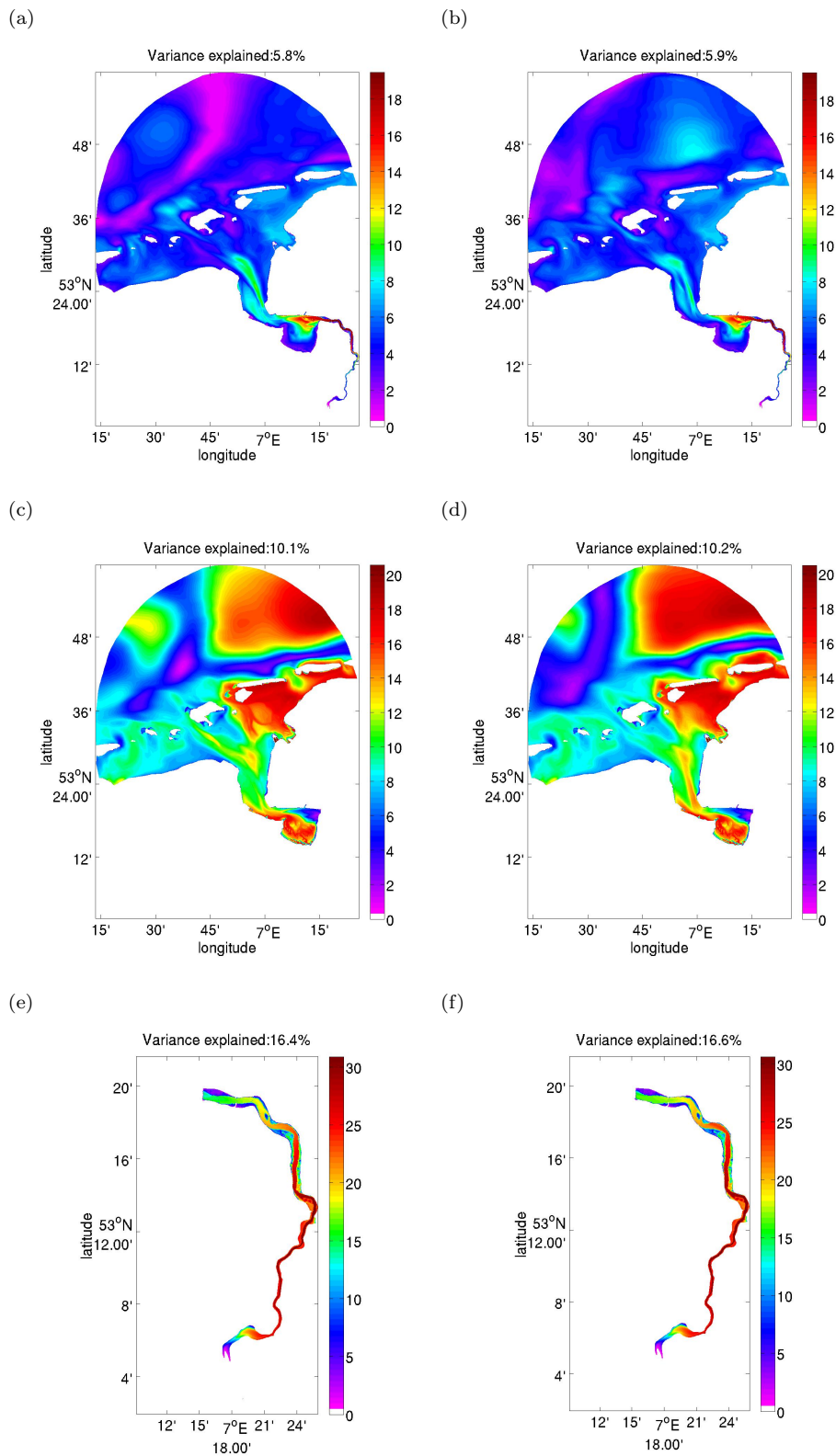
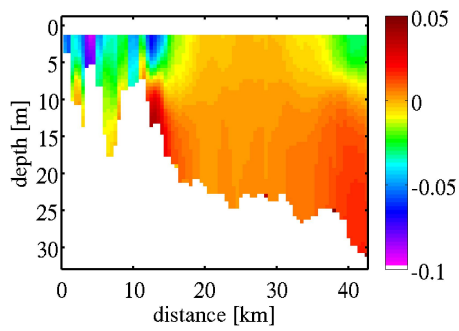
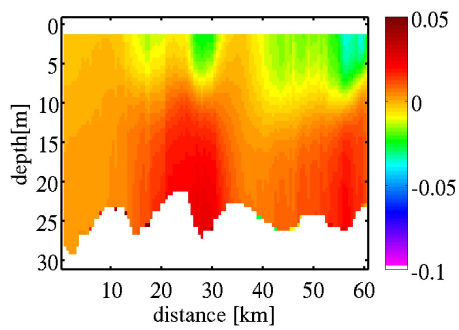


Fig. 11: Footprint of observations locations on the correlation structure within the model area for (a) the bottom layer and (b) the surface layer; outer estuary (c,d); tidal river (e,f).

(a)



(b)



(c)

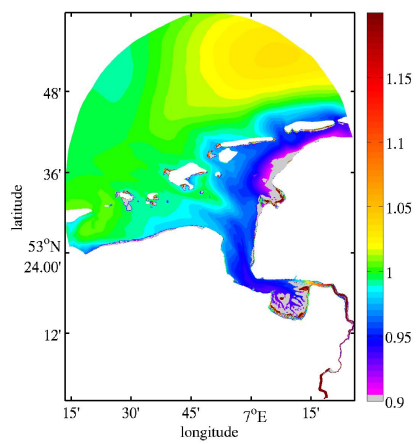


Fig. 12: The time-averaged salinity anomalies [psu] along the (a) meridional and (b) zonal transect lines in Fig. 1b. The anomalies have been calculated as deviations from the vertically-averaged salinity. The data has been sampled from 24 h of model results beginning on the 8th June 2012. (c) The ratio between mean spring sea-surface salinity and mean neap sea-surface salinity.

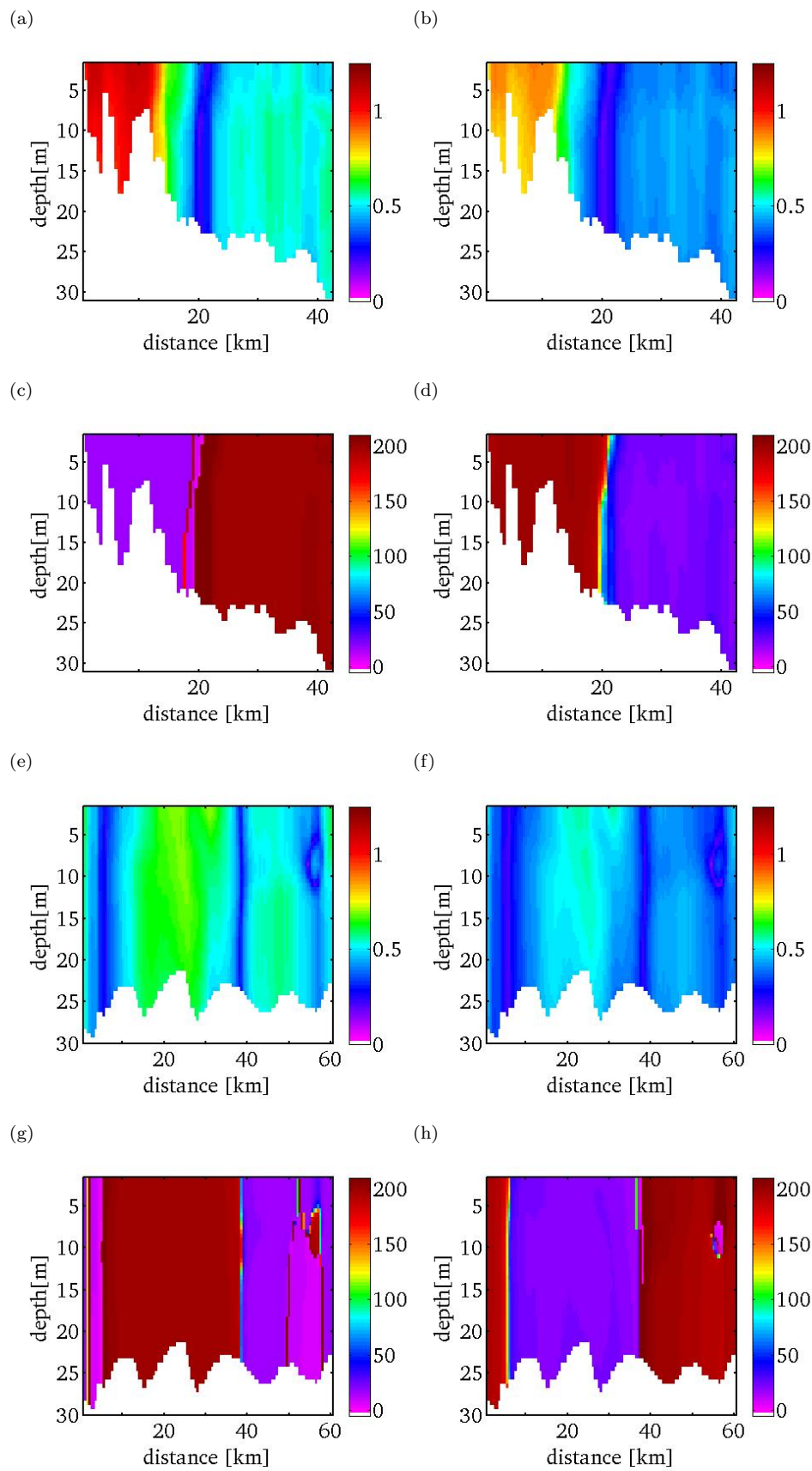


Fig. 13: The amplitudes [m] and phases [°] of the M-2 (a,c; e,g) and M-4 (b,d; f,h) tidal variations of the 3D salinity field along meridional (a-d) and zonal (e-h) transect lines in Fig. 1b)